MAMMOTH: confirmation of two massive galaxy overdensities at $z = 2.24$ with Hα emitters

Xian Zhong Zheng [1,2]★ Zheng Cai,[3]★ Fang Xia An,[4] Xiaohui Fan[5] and Dong Dong Shi[1,2,5]

[1]*Purple Mountain Observatory, Chinese Academy of Sciences, 10 Yuanhua Road, Nanjing 210023, China*
[2]*School of Astronomy and Space Sciences, University of Science and Technology of China, Hefei 230026, China*
[3]*Department of Astronomy, Tsinghua University, Beijing 100084, China*
[4]*Inter-University Institute for Data Intensive Astronomy, and Department of Physics and Astronomy, University of the Western Cape, Robert Sobukwe Road, Bellville 7535, Cape Town, South Africa*
[5]*Steward Observatory, University of Arizona, 933 N. Cherry Ave., Tucson, AZ 85721, USA*

ABSTRACT

Massive galaxy overdensities at the peak epoch of cosmic star formation provide ideal testbeds for the formation theories of galaxies and large-scale structure. We report the confirmation of two massive galaxy overdensities at $z = 2.24$, BOSS1244 and BOSS1542, selected from the Mapping the Most Massive Overdensities Through Hydrogen (MAMMOTH) project using Lyα absorption from the intergalactic medium over the scales of $15-30\,h^{-1}$ Mpc imprinted on the quasar spectra. We use Hα emitters (HAEs) as the density tracer and identify them using deep narrow-band $H_2S(1)$ and broad-band K_s imaging data obtained with the wide-field infrared camera (WIRCam) at the Canada–France–Hawaii Telescope. In total, 244 and 223 line emitters are detected in these two fields, and 196 ± 2 and 175 ± 2 are expected to be HAEs with an Hα flux of $>2.5 \times 10^{-17}\,\mathrm{erg\,s^{-1}\,cm^{-2}}$ (corresponding to a star formation rate of $>5\,\mathrm{M_\odot\,yr^{-1}}$). The detection rate of HAE candidates suggests an overdensity factor of $\delta_{\mathrm{gal}} = 5.6 \pm 0.3$ and 4.9 ± 0.3 over the volume of $54 \times 32 \times 32$ co-moving Mpc^3. The overdensity factor increases two to three times when focusing on the high-density regions of scales 10–15 co-moving Mpc. Interestingly, the HAE density maps reveal that BOSS1244 contains a dominant structure, while BOSS1542 manifests as a giant filamentary structure. We measure the Hα luminosity functions (HLFs), finding that BOSS1244's HLF is nearly identical to that of the general field at the same epoch, while BOSS1542 shows an excess of HAEs with high Hα luminosity, indicating the presence of enhanced star formation or active galactic nuclei activity. We conclude that the two massive MAMMOTH overdensities are undergoing a rapid galaxy mass assembly.

Key words: galaxies: clusters: individual: BOSS1244 – galaxies: clusters: individual: BOSS1542 – galaxies: high-redshift – quasars: absorption lines – galaxies: star formation.

1 INTRODUCTION

Understanding the formation of galaxy clusters is a central task in modern astrophysics (Berrier et al. 2009; Allen, Evrard & Mantz 2011). While the standard ΛCDM model is successful at reproducing the dark matter driven perspective of cluster formation (e.g. the abundance and clustering properties), the physical processes that regulate the mass assembly of cluster member galaxies, and influence the baryons within a cluster through feedback, have yet to be fully understood (Kravtsov & Borgani 2012; Schaye et al. 2015). Compared with the general field, galaxy clusters contain more massive galaxies and amplify details of these baryonic processes, including gas cooling, star formation, stellar feedback, black hole activity, galaxy merging and environmental effects, thus making them unique testbeds for theoretical models of galaxy formation (Overzier 2016).

It has long been known that the dense environment of galaxy clusters dramatically affects galaxy properties. The massive early-type galaxies in the clusters tend to form at earlier epochs, indicating that their progenitors would be actively star-forming galaxies (SFGs) in galaxy protoclusters at $z \gtrsim 2$–3 (Thomas et al. 2005). Indeed, cluster galaxies have lower star formation rates (SFRs) than field galaxies in the local Universe (e.g. Dressler 1984; Kauffmann et al. 2004; Blanton & Moustakas 2009; von der Linden et al. 2010; Owers et al. 2019), while this trend is found to be reversed at $z > 1$ (Elbaz et al. 2007; Tanaka et al. 2010; Koyama et al. 2013; Dannerbauer et al. 2014; Tran et al. 2015; Umehata et al. 2015; Hayashi et al. 2016; Shimakawa et al. 2018a). A higher fraction of active galactic nuclei (AGNs) was reported in some $z \sim 1$–3 protoclusters, compared with the general field at the same epoch, indicating an enhanced growth of supermassive black holes (SMBHs) in the high-density environment (Lehmer et al. 2009; Digby-North et al. 2010; Martini et al. 2013; Krishnan et al. 2017). Similarly, the fraction of galaxy mergers (Hine et al. 2016; Watson et al. 2019) and the galaxy gas fraction (Noble et al. 2017; Coogan et al. 2018) are likely to be higher in $z > 2$ protoclusters, although the fraction of massive gas-rich SFGs in the central regions of protoclusters depends on their evolutionary stage (Casey et al. 2015; Wang et al. 2018; Shimakawa et al. 2018a; Zavala

★ E-mail: xzzheng@pmo.ac.cn (XZZ); zcai@mail.tsinghua.edu.cn (ZC)

et al. 2019). Nevertheless, how these distant SFGs evolve into local massive galaxies in different cluster environments is still not yet clear (e.g. De Lucia & Blaizot 2007; Lidman et al. 2012; Contini et al. 2016; Casey 2016; Shimakawa et al. 2018b). In particular, where and how different environmental interactions play roles in shaping galaxy properties remain open questions. Galaxy protoclusters at the peak epoch of cosmic star formation and black hole growth ($z \sim$ 2–3; Madau & Dickinson 2014) provide a useful probe of the rapid mass assembly of galaxies in relation to structure formation (Bond, Kofman & Pogosyan 1996; Boylan-Kolchin et al. 2009; Brodwin et al. 2013; Chiang et al. 2017). Investigating massive protoclusters and the properties of their member galaxies at this peak epoch will provide key constraints on the environmental dependence of the galaxy evolution and black hole growth.

A protocluster refers to an unvirialized structure of all the dark matter and baryons that will assemble into a present-day galaxy cluster. Galaxy protoclusters at $z > 2$ are expected to have an average overdensity of $\rho/\bar{\rho} \approx 2$ over a scale of $\gtrsim 20\,h^{-1}$ co-moving Mpc (cMpc; Muldrew, Hatch & Cooke 2015; Lovell, Thomas & Wilkins 2018). In practice, it is possible to identify galaxy overdensities of a given scale at high redshift but whether they are protoclusters depends on the scale and their surrounding gravitational environments. Generally, massive overdensities over large scales of $\gtrsim 10$–$30\,h^{-1}$ cMpc naturally represent protoclusters while small-scale overdensities may be either the progenitors of local groups or part of the protoclusters. Yet, a number of $z > 2$ protoclusters have been spectroscopically identified. However, few of them were initially identified as massive overdensities at a scale of $\gtrsim 20\,h^{-1}$ cMpc. These protoclusters have been selected by various means and thus are often biased by selection effects (e.g. Shi et al. 2019). Deep cosmic surveys are used to detect protoclusters at high redshift (e.g. Cucciati et al. 2014; Lemaux et al. 2014; Yuan et al. 2014; Chiang et al. 2015; Tran et al. 2015; Toshikawa et al. 2016; Wang et al. 2016). Rare massive sources, such as quasars or bright radio galaxies, usually reside in dense environments and can also be used as protocluster indicators (Venemans et al. 2007; Hayashi et al. 2012; Onoue et al. 2018). Surveys for galaxy clusters relying on either the Sunyaev–Zel'dovich (SZ) effects (Bleem et al. 2015) or the excess of red-sequence galaxies (Gilbank et al. 2011; Strazzullo et al. 2016) are biased to pick up relaxed clusters, mostly at $z < 1.5$, containing hot gas and/or a large fraction of quenched massive galaxies. The sample of confirmed protoclusters at $z = 2$–4 selected by these approaches are incomplete and difficult to use for statistical comparisons with hierarchical models of structure formation (Chiang, Overzier & Gebhardt 2013). Moreover, the evolution of the most massive haloes at high redshift are essentially determined by the surrounding density field on large scales of $\gtrsim 10\,h^{-1}$ cMpc (Angulo et al. 2012). The identified protoclusters at small scales might not necessarily evolve into present-day massive clusters.

The Lyα forest optical depth is predicted to be strongly correlated with dark matter overdensity at scales of $\gtrsim 3\,h^{-1}$ cMpc and the correlation peaks at 10–30 h^{-1} cMpc (e.g. Kollmeier et al. 2003). Cai et al. (2016) demonstrated with simulations that the intergalactic medium (IGM) traces the underlying dark matter density field, and the strongest IGM Lyα absorptions mostly trace massive overdensities at the scale of 15 h^{-1} cMpc. Based on this correlation, a novel approach – the Mapping the Most Massive Overdensities Through Hydrogen (MAMMOTH) project – has been developed for identifying such mass/galaxy overdensities at $z = 2$–3, traced by groups of coherently strong Lyα absorption (CoSLA) imprinted on the spectra of a number of background quasars (Cai et al. 2016). This method is inherently less biased than many other techniques because the H I density is

closely correlated with matter density over large scales. It also covers a much larger survey volume, when using the large quasar absorption-line data base from spectroscopic surveys such as the Sloan Digital Sky Survey (SDSS) and the Baryon Oscillation Spectroscopic Survey (BOSS). This technique has been successfully confirmed with the discovery of the BOSS1441 protocluster at $z = 2.32$ using the early data release of SDSS-III (Cai et al. 2017). The spectroscopic data base from SDSS-III allows us to search for more massive overdensities of scales of 10–30 h^{-1} cMpc over dramatically larger volumes.

We aim to construct a statistical sample of MAMMOTH overdensities and to fully quantify and characterize their member galaxies. We use a pre-existing narrow-band filter $H_2S(1)$ to detect Hα emitters (HAEs) at $z = 2.24$, which resulted in the selection of two $z = 2.24$ overdensities traced by extreme groups of IGM Lyα absorption systems from SDSS-III quasar spectra. In this work, we present the results of confirmation of the two massive overdensities with HAEs. A detailed analysis of member Hα emission-line galaxies will be presented in a subsequent paper (Shi et al., in preparation). The selection of a sample of MAMMOTH overdensities and implications to the formation of cosmic structures will be given in Cai et al. (in preparation).

In Section 2, we introduce how the two targets are selected. In Section 3, we present the near-infrared imaging observations and data reduction. Our results are given in Section 4. We discuss and summarize our results in Section 5. A standard ΛCDM cosmology with $H_0 = 70$ km^{-1} Mpc^{-1}, $\Omega_\Lambda = 0.7$ and $\Omega_m = 0.3$ and a Kroupa (2001) initial mass function (IMF) are adopted throughout the paper. All magnitudes are referred to the AB system unless mentioned otherwise.

2 SELECTION OF TWO $z = 2.24$ MAMMOTH TARGETS

Our goal is to confirm the massive overdensity candidates from MAMMOTH using Hα emission-line objects at $z = 2.246 \pm 0.021$ selected from the narrow-band $H_2S(1)$ ($\lambda_c = 2.130\,\mu$m, $\Delta\lambda = 0.0293\,\mu$m) and broad-band K_s filters on the Wide-field InfraRed Camera (WIRCam) at the Canada–France–Hawaii Telescope (CFHT). The MAMMOTH overdensities are selected using the IGM Lyα forest absorption systems from the SDSS-III (Alam et al. 2015) over a sky coverage of 10 000 deg². To match the $H_2S(1)$ filter, only the deep IGM absorption with the redshift range of $z = 2.246 \pm 0.021$ is used.

Following Cai et al. (2016), the deep Lyα absorbers are selected by selecting regions where the effective optical depth ($\tau_{\rm eff}$) over 15 h^{-1} Mpc (= 15 Å) is four times higher than the mean optical depth at $z = 2.2$. Using the selection criteria described in detail in Cai et al. (in preparation), we removed the contaminant DLAs, which also cause large equivalent width (EW) absorption based on the Lyα absorption profiles. We then select the fields with the highest density of deep IGM absorption. From the complete SDSS-III quasar data base, we identified two target fields, BOSS1244 and BOSS1542, suitable for observing during the spring and summer months. The two fields have groups of IGM strong absorption systems comparable to those in the BOSS1441 field (Cai et al. 2017). They also contain several quasi-stellar objects (QSOs; i.e. quasars) at the same redshift. Figs 1 and 2 present the effective optical depth $\tau_{\rm eff}$ along the line of sight derived from strong Lyα absorption lines by absorbers at $z \sim 2.24$ imprinted on quasar spectra in the two selected fields. These absorbers probed by background quasars spread over a scale of 15 h^{-1} Mpc.
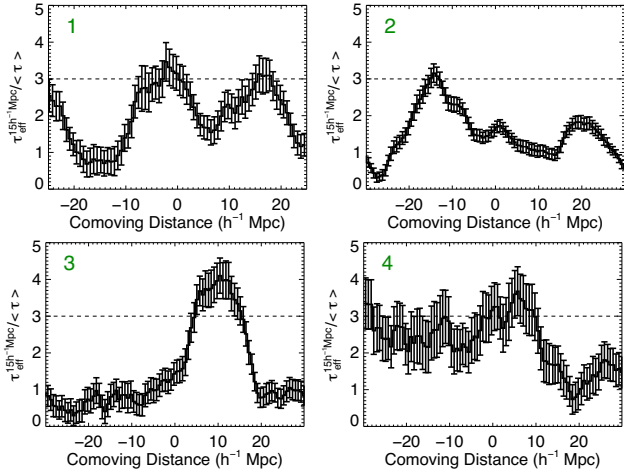
Figure 1. Effective optical depth (τ_{eff}) derived from Lyα absorption lines at $z \sim 2.24$ imprinted on the spectra of four quasars in the BOSS1244 field.
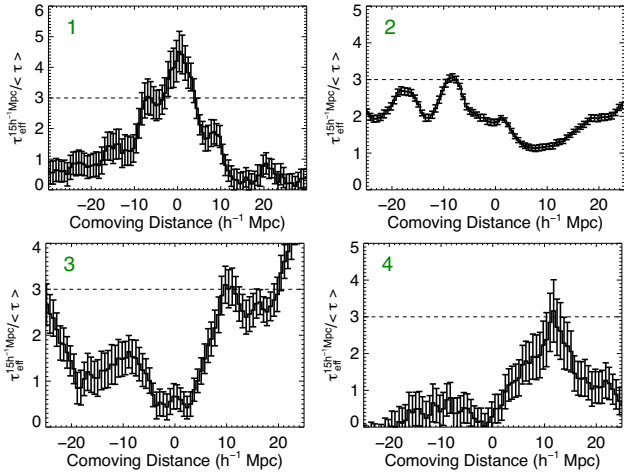
Figure 2. Effective optical depth (τ_{eff}) derived from Lyα absorption lines at $z \sim 2.24$ imprinted on the spectra of four quasars in the BOSS1542 field.

3 OBSERVATIONS AND DATA REDUCTION

We used WIRCam on board the CFHT to obtain deep near-infrared (NIR) imaging of the two MAMMOTH fields in both the narrow-band $H_2S(1)$ ($\lambda_c = 2.130\,\mu m$, $\Delta\lambda = 0.0293\,\mu m$) and broad-band K_s ($\lambda_c = 2.146\,\mu m$, $\Delta\lambda = 0.3250\,\mu m$) filters (PI: FX An). The observations were carried out with the regular QSO mode under a median seeing of $0.65-0.8$ arcsec. WIRCam has a field of view (FOV) of 20×20 arcmin^2, covered by four 2048×2048 HAWAII2-RG detectors with a pixel scale of 0.3 arcsec pixel^{-1}. The gaps between detectors are 45 arcsec. The observations were dithered to cover gaps between detectors and to correct for bad pixels. We centred the FOV of WIRCam at the centres of BOSS1244 (RA = 12:43:55.49, Dec. = +35:59:37.4) and BOSS1542 (RA = 15:42:19.24, Dec. = +38:54:14.1) for the epoch of J2000.0. The total integration times are 7.18 and 4.96 h for the $H_2S(1)$ and K_s observations in BOSS1244, and 7.275 and 5.17 h for the $H_2S(1)$ and K_s observations in BOSS1542, respectively. Each exposure takes 190 s for the $H_2S(1)$
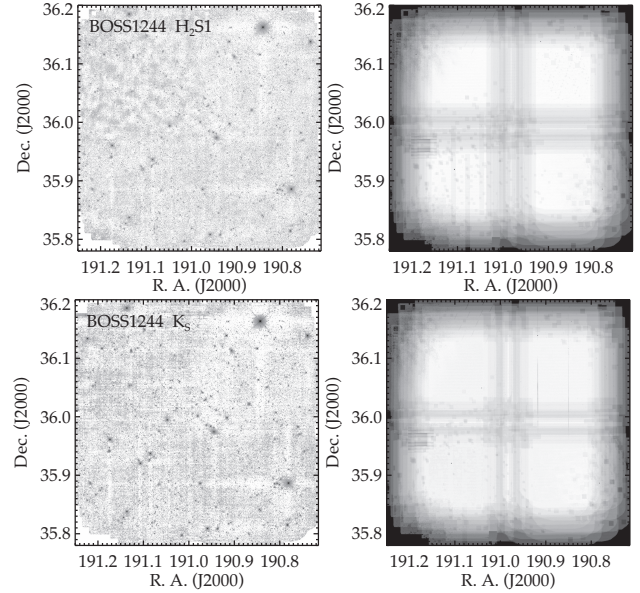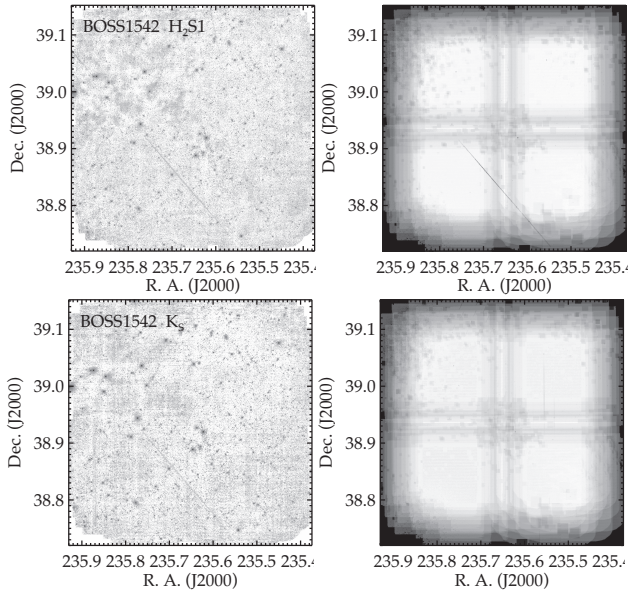
Figure 3. Science image (left) and exposure map (right) taken with the CFHT/WIRCam through the narrow-band $H_2S(1)$ (top) and broad-band K_s (bottom) filters for the overdensity field BOSS1244.

filter (194 s in BOSS1542) and 20 s for the K_s filter. Accounting for the overall overhead time (10 s per exposure), the total observing time is 7.50 h for each of the two bands in BOSS1244, and 7.65 h for $H_2S(1)$ and 7.75 h for K_s in BOSS1542. In total, 30.40 h of telescope time were used in our observing programme of two MAMMOTH fields.

The data reduction was carried out following An et al. (2014). The reduced $H_2S(1)$ and K_s images were calibrated in astrometry using compact sources from the SDSS. In total, ~ 700 SDSS compact sources with $12.0 < z < 20.5$ mag in the BOSS1244 field and 1985 compact sources with $12.0 < z < 20.5$ mag in the BOSS1542 field are used for astrometric calibration, giving an astrometric accuracy of ~ 0.1 arcsec. Co-adding 136/893 and 135/930 frame $H_2S(1)/K_s$ science images produced the final science images and the exposure time maps in BOSS1244 and BOSS1542, respectively. The point sources from the 2MASS catalogue are used to perform photometric calibration. In total, 186 and 283 point sources with $12.6 < K_s < 15.5$ mag in the two fields are selected for photometric calibration. An empirical point spread function (PSF) is built from these stars and used to derive aperture correction. The photometric calibration reaches an accuracy of 1 per cent for the selected stars in our mosaic $H_2S(1)$ and K_s images.

All final science images of the two MAMMOTH fields show a similar PSF with full width at half-maximum (FWHM) of 0.78 ± 0.01 arcsec. Figs 3 and 4 present the $H_2S(1)$ and K_s science images and corresponding exposure maps for BOSS1244 and BOSS1542, respectively. The effective area with a total integration time of $> 0.5 \times$ maximum is 417 and 432 arcmin^2 for $H_2S(1)$ and K_s in BOSS1244, and 399 and 444 arcmin^2 for $H_2S(1)$ and K_s in BOSS1542, respectively. The image depth (5σ, AB for point sources) within the effective area is estimated through random photometry on a blank background using an aperture of 2-arcsec diameter, giving $H_2S(1) = 22.58$ mag and $K_s = 23.29$ mag for BOSS1244 and $H_2S(1) = 22.67$ mag and $K_s = 23.23$ mag for BOSS1542.

Figure 4. Science image (left) and exposure map (right) taken with the CFHT/WIRCam through the narrow-band $H_2S(1)$ (top) and broad-band K_s (bottom) filters for the overdensity field BOSS1542.

4 RESULTS

4.1 Identifying emission-line objects

We select emission-line objects through narrow-band $H_2S(1)$ + broad-band K_s imaging with the CFHT/WIRCam in two 20 × 20 arcmin^2 fields of MAMMOTH overdensities. The software SEXTRACTOR (Bertin & Arnouts 1996) is used for source detection and flux measurement in the $H_2S(1)$ image. A secure source detection is based on at least five contiguous pixels that contain fluxes above three times the background noise ($\geq 3\sigma$). The exposure map is used as the weight image to suppress false sources in the low signal-to-noise (S/N) area. The $H_2S(1)$ and K_s images are aligned into the same frame. Photometry is carried out using SEXTRACTOR under the dual-image mode, in which the flux of a source in the K_s image is measured over the same area as in the H_2S1 image. We limit source detection in the area with a 5σ depth down to $H_2S(1) = 22.58$ mag for BOSS1244 and $H_2S(1) = 22.67$ mag for BOSS1542. The same detection area in K_s reaches a depth of $K_s = 23.29$ and 23.23 mag, respectively. In total, 6253 and 8012 sources are securely detected with an S/N ratio of >5 in the $H_2S(1)$ image of BOSS1244 and BOSS1542, respectively.

The presence of a strong emission line induces a flux excess in the narrow band relative to the broad band. We use $K_s - H_2S(1)$ to select emission-line objects as

$$K_s - H_2S(1) > -2.5 \log \left(1 - \Sigma \sqrt{\sigma_{K_s}^2 + \sigma_{H_2S(1)}^2} / f_{H_2S(1)} \right), \quad (1)$$

where Σ is the significant factor, and $\sigma_{H_2S(1)}$ and σ_{K_s} are $H_2S(1)$ and K_s background noises. Here, the $H_2S(1)$-band flux is defined as $f_{H_2S(1)} = 0.3631 \times 10^{0.4\,[25 - H_2S(1)]}$. The background noises and $f_{H_2S(1)}$ are given in units of μJy. Fig. 5 shows the colour $K_s - H_2S(1)$ as a function of $H_2S(1)$ magnitude for sources detected in BOSS1244 and BOSS1542. We adopt $\Sigma > 3$ to identify emission-line objects. The strength of an emission line is quantified by the rest-frame EW. Here, a cut of EW > 45 Å is adopted to minimize false excess caused by the photon noises of bright objects. This cut corresponds

to $K_s - H_2S(1) > 0.39$ mag. A lower EW cut (e.g. EW > 30 Å) will increase only a few more candidates and thus have marginal effect on our results.

From Fig. 5, 251 and 230 emission-line candidates are selected with $\Sigma > 3$, EW > 45 Å and $H_2S(1) < 22.5$ mag in BOSS1244 and BOSS1542, respectively. We visually examined these candidates and removed 7/7 of the 251/230 false sources in the two fields. These are either spikes of bright stars or contaminations. In the end, 244 and 223 emission-line objects are identified in BOSS1244 and BOSS1542, respectively. Among these emission-line objects, five in BOSS1244 and three in BOSS1542 are spectroscopically confirmed as QSOs at $z \sim 2.24$ in the SDSS.

The emission lines in the $H_2S(1)$ filter may be Hα at $z = 2.24$, Paα at $z = 0.14$, [Fe II] at $z = 0.30$, Paβ at $z = 0.66$, [S III] at $z = 1.23/1.35$ and [O III] at $z = 3.25$. By limiting the $H_2S(1)$ and K_s data from An et al. (2014) to the depths of our observations, we estimate that about 78 emitters would be detected over 383 arcmin^2 of the Extended Chandra Deep Field South (ECDFS). Of these emitters, 36–40 per cent are HAEs (Hayes, Schaerer & Östlin 2010; Lee et al. 2012; An et al. 2014), suggesting a number density of 31–34 over 417 arcmin^2 for HAEs in the general field. The numbers of emitters we detect in the two MAMMOTH fields are much higher, undoubtably contributed by an excess of HAEs at $z = 2.24$. This is strongly supported by the fact that a group of CoSLAs at $z \sim 2.24$, as a convincing tracer of overdensities, are probed by background quasars, as well as the fact that these spectroscopically identified QSOs are also detected as emitters at the same redshift (i.e. $z = 2.24$). Moreover, the possibility that the excess of emitters is associated with other redshift slices is negligible. We point out that the volume is too small to contain a significant number of Paα emitters at $z = 0.14$ or [Fe II] emitters at $z = 0.30$. The strong [S III] emission lines are usually powered by shock waves in the post-starburst phase (An et al. 2013). As we will show later, the excess is contributed by an overdensity of $\delta_{gal} > 5$, where $\delta_{gal} = (\Sigma - \Sigma_{field})/\Sigma_{field}$. It is hard to believe that a large number of SFGs in such massive overdensities at $z = 1.23/1.35$ could turn them into the post-starburst phase in a locked step. The excess of emitters is unlikely to be associated with overdensities at $z = 3.25$ traced by [O III] emitters because no $z \sim 3.25$ CoSLAs are found from the spectra of the background quasars. We caution that the weak overdensities at $z = 1.23/1.35$ or $z = 3.25$, if they exist, might still contaminate the identification of substructures in the HAE-traced overdensities at $z = 2.24$ unless these emitters are identified with spectroscopic redshifts.

We aim to estimate the total number of HAEs detected in our fields. It is clear that the detection rate of HAEs is sensitive to the image depths and cosmic variance. The data sets in the ECDFS suggest 78 emitters (33 HAEs and 45 non-HAEs) can be detected over 383 arcmin^2 using our selection criteria. We note that this likely overestimates the emitter detection rate because the detection completeness is higher in the deeper ECDFS observations. Instead, we adopt 78 emitters detected over the survey area of 417 arcmin^2 in BOSS1244, giving a detection rate of 0.187 per arcmin^2. We adopt 36–40 per cent of the emitters as HAEs (Hayes et al. 2010; Lee et al. 2012; An et al. 2014), giving a detection rate of 0.071 ± 0.004 per arcmin^2 for HAEs at $z = 2.24$ and 0.116 ± 0.004 per arcmin^2 for non-HAEs. We obtain 48 ± 2 non-HAEs and 30 ± 2 HAEs over the same area in the general field. We use these two numbers for both of our two fields and ignore the variation in survey area. Of 244/223 emission-line objects, we estimate the number of HAEs at $z = 2.24$ to be 196 ± 2 and 175 ± 2 in BOSS1244 and BOSS1542, respectively, yielding an overdensity factor $\delta_{gal} = 5.6 \pm 0.3$ for BOSS1244 and 4.9 ± 0.3 for BOSS1542. Here, the errors account
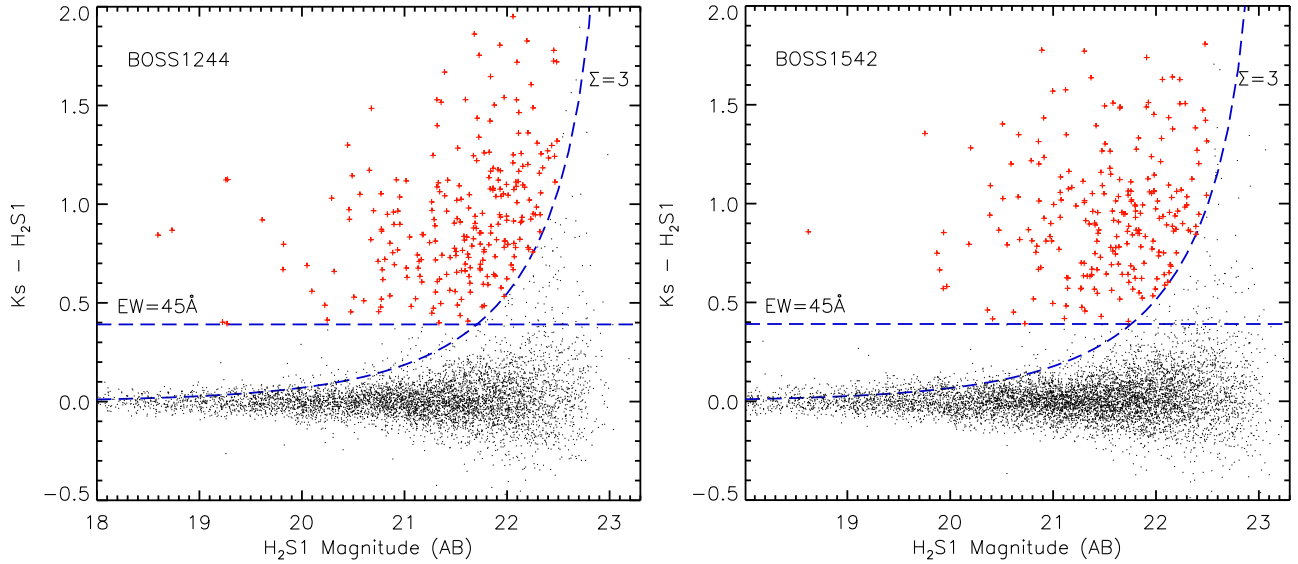
Figure 5. Selection diagram of $H_2S(1)$ magnitude versus $K_s-H_2S(1)$ for emission-line candidates in BOSS1244 (left) and BOSS1542 (right). The dashed curves refer to the selection limitation given in equation (1) with a signification level of $\Sigma = 3$. The horizontal dashed lines represent rest-frame EW $= 45$ Å ($H_2S(1)-K_s = 0.39$ mag). The selection criteria pick up 244 (left) and 223 (right) emission-line objects with $H_2S(1) < 22.5$ mag. Of them, ~196 and 175 are estimated to be true HAEs at $z = 2.24$ after correcting for foreground and background emitters, respectively.

only for the variation in the fraction of HAEs in the general field. The uncertainty in the detection rate of emitters is mostly driven by the cosmic variance and not counted here. We notice that there are only 21/28 objects in the low-density regions of BOSS1244 and BOSS1542, giving an emitter detection rate of 0.124 and 0.135 per arcmin^2, respectively (see the next subsection for more details) slightly lower than the adopted value (0.187 per arcmin^2). This hints that the cosmic variance may induce an uncertainty up to 50 per cent. As the fraction of HAEs in the low-density regions is unknown, we choose the ECDFS as a representative for the general field. We point out that decreasing the detection rate for the general field will increase the overdensity factors that we estimated, and further strengthen our conclusions. When focusing on the high-density regions (see Fig. 6), the overdensity factor increases by two to three times.

The redshift slice of $z = 2.246 \pm 0.021$ over 20×20 arcmin^2 corresponds to a co-moving box of $54.3 \times 32.0 \times 32.0$ ($= 55\,603$) h^{-3} cMpc^3, equal to a cube of $38.2\,h^{-1}$ cMpc each side. The overdensity factor of $\delta_{gal} \sim 5-6$ over such a large scale displays the overdensities in our two target fields as most massive at the epoch of $z \sim 2-3$ (Cai et al. 2016). We thus conclude that the large excess of HAEs confirms BOSS1244 and BOSS1542 as massive overdensities at $z = 2.24$. The confirmation validates the effectiveness of the MAMMOTH technique in identifying the massive overdensities of scales $15 - 30\,h^{-1}$ Mpc at $z \sim 2-3$. We note that the redshift slice is given by the width of the $H_2S(1)$ filter that corresponds to a line-of-sight distance of 54.3 cMpc at $z = 2.24$. This scale should be sufficiently large for the detection of the progenitor of local clusters such as the Coma (Chiang et al. 2013), although there is still a possibility that some galaxies of the overdensities might spread out of the redshift slice (e.g. a protocluster across ~60 cMpc in the SSA22 field; Matsuda et al. 2005) possibly partially due to the Fingers of God effect caused by the peculiar velocities of galaxies. A complete census of these massive overdensities will require spectroscopic surveys of galaxies over a larger sky coverage and wider range in redshift to map the kinematics of the overdensities and their surrounding density fields.

4.2 Density maps of Hα emitters

We estimate that 196 of 244 (80 per cent) and 175 of 223 (78 per cent) emission-line objects are HAEs at $z = 2.24$ that belong to the massive overdensities BOSS1244 and BOSS1542, respectively. The non-HAEs are located at foreground or background of the $z = 2.24$ slice. In the ECDFS field, non-HAEs consist of 42 per cent foreground and 58 per cent background emitters (i.e. [O III] emitters at $z = 3.25$), when limiting the detection to the depths of the BOSS1244 observations. It is expected that these non-HAEs spread randomly over the observed area. We thus use all emitters to build the density map and the presence of non-HAEs can be seen as a flat density layer in a statistical manner. We adopt the number density of 0.116 per arcmin^2 for non-HAEs and of 0.071 per arcmin^2 for $z = 2.24$ HAEs in the general field. We note that galaxies reside in the cosmic web, so we cannot exclude the possibility that the foreground or background non-HAEs might associate with some structures and contaminate the density maps of HAEs at $z = 2.24$.

We identified the emission-line objects in the high-S/N regions, corresponding to an area of 20×20 arcmin^2 in each field. We treat each object equally and use the projected number density of all emitters to trace the projected matter density. The detection area is divided into a grid of cells with 1.2×1.2 arcmin^2 each, and the number of emitters in each cell region is then counted to generate a density map. A Gaussian kernel of $\sigma = 1$ arcmin (1.6 cMpc at $z = 2.246$) is utilized to convolve the density map. Contours of density maps are drawn at the levels of 4, 8, 12, 16, 20 and 24 times the number density of HAEs of the general field (0.071 per arcmin^2) plus the number density of non-HAEs (0.116 per arcmin^2). Fig. 6 shows the spatial distributions of emission-line objects in two MAMMOTH fields, overplotted with the density maps. The contours in two density maps are given in identical levels in order to compare these two fields. Out of the first contour level lines, there are only 21 and 28 objects over 169 and 207 arcmin^2 in BOSS1244 and BOSS1542, respectively, giving an emitter detection rate of 0.124 and 0.135 per arcmin^2 in 41 and 52 per cent of the total area of the two fields. These
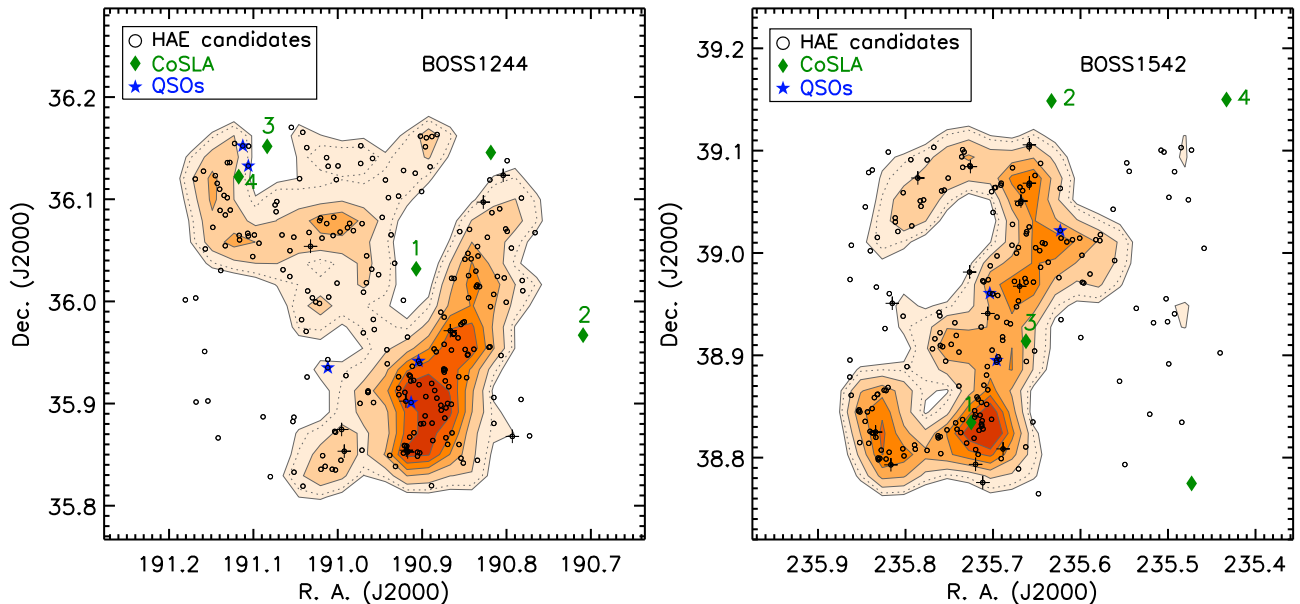
Figure 6. Density maps of HAE candidates in BOSS1244 (left) and BOSS1542 (right). Black circles represent the selected emission-line candidates. A Gaussian kernel of $\sigma = 1$ arcmin (1.6 cMpc at $z = 2.246$) is adopted to smooth the density maps and draw the contours in the same linear scale. The contour levels refer to [4, 8, 12, 16, 20, 24] times the number density of HAEs in the general field (0.071 per arcmin^2). The dotted lines mark the contour level of 5.2×0.071 per arcmin^2 used as the boundaries between the outskirts and dense regions. A group of CoSLAs (green diamonds) and QSOs (blue stars) at $z \simeq 2.24$ are marked. Green numbers mark CoSLAs shown in Figs 1 and 2. Black crosses pinpoint the emitters with highest line fluxes ($\log L_{H\alpha} > 43.4$). The HAE-traced density maps uncover that the two massive overdensities have different structures: BOSS1244 is dominated by an elongated high-density structure, and BOSS1542 appears to be a large-scale filamentary structure.

values indicate that the number density of non-HAEs (~60 per cent of the total) is likely to be significantly lower than that in the ECDFS.

It is clear from Fig. 6 that the density maps traced by HAEs reveal substructures of the two massive overdensities. BOSS1244 exhibits two components within the observed area: a low-density component connected to an elongated high-density component with a scale of 25×10 cMpc. The high-density component spreads over an area of 103 arcmin^2 within the first contour level and reaches an overdensity factor of $\delta_{gal} \sim 15$, and even ~ 24 in the central 4×6 arcmin^2 region. The massive overdensities of $\delta_{gal} > 6$ traced by star-forming galaxies over $(15 \text{ cMpc})^3$ are predicted by simulations exclusively to be protoclusters; that is, the progenitors of massive galaxy clusters of $>10^{15}$ M$_\odot$ (e.g. the Coma cluster) in the local Universe (Chiang et al. 2013). One caveat is that the elongated structure in BOSS1244 might be extended or divided into multiple components along line of sight over 54.3 cMpc. Even if we divide the overdensity factor $\delta_{gal} \sim 15$ by three to match the volume of $(15 \text{ cMpc})^3$, the divided structures would be still sufficiently massive and overdense to form massive clusters.

In contrast, BOSS1542 can be seen as a large-scale filamentary structure with multiple relatively dense clumps. The density and size of these clumps are significantly smaller than the dominant component of BOSS1244. The total length of the structure along the filament reaches 50 cMpc. This structure covers an area of 192 arcmin^2 (~32×15 cMpc at $z = 2.246$) and yields $\delta_{gal} \sim 10$ within the first contour level shown in Fig. 6. The bottom part at Dec. < 38.88 spread over 72 arcmin^2 (~12×15 cMpc at $z = 2.246$) and have a mean $\delta_{gal} \sim 11$. We suspect that at least part of the filamentary structure could eventually condense into one massive galaxy cluster as revealed by simulations (e.g. Chiang et al. 2013). Spectroscopic observations can map kinematics of member galaxies and quantitatively determine if different components in these overdensities could merge into one mature cluster of galaxies. We

will carry out a detailed analysis of dynamics and masses for the two HAE-traced overdensites using spectroscopic data in a companion work (Shi et al., in preparation).

We notice that the density maps of our two HAE-traced structures might be contaminated by the foreground or background emitters that are probably associated with overdensities. We examine the possibility by comparing the line flux distributions of those emitters in dense regions and outskirts. Out of the first contour level lines, there are only 21 and 28 objects in BOSS1244 and BOSS1542, respectively. We adopt the contour lines at the level of 5.2×0.071 per arcmin^2 (the dotted lines in Fig. 6) as the boundaries of the dense regions to ensure that the outskirts contain ~40 objects sufficient for a meaningful statistics and to avoid serious contamination from the dense regions at the same time. In BOSS1244, the dense regions include two parts: left density and right density (i.e. the elongated structure). In BOSS1542, HAEs form a giant filamentary structure. We split the dense regions into two roughly equal parts via a horizontal line at Dec. = 38.92 (i.e. top density and bottom density). Fig. 7 shows the cumulative curves of line fluxes in different parts of the two MAMMOTH fields. Here, five QSOs in BOSS1244 and three QSOs in BOSS1542 are excluded. For comparison, we present the cumulative curves for the HAEs at $z = 2.24$ and non-HAEs (i.e. foreground and background emitters) in the ECDFS from An et al. (2014). These emitters are selected at the same detection depths as our BOSS1244 observations.

It is clear from Fig. 7 that in the ECDFS the observed line fluxes of the HAEs at $z = 2.24$ are systematically higher by 0.1 dex than those of the non-HAEs. We note that the 45 non-HAEs include 26 [O III] emitters at $z = 3.25$ that appear globally fainter than HAEs at $z = 2.24$. In BOSS1244, the right density (i.e. the elongated dominant structure in Fig. 6) contains emitters with line fluxes relatively higher than the emitters in the outskirts; the left density shows a cumulative curve similar to that of the outskirts. It is worth noting that the left
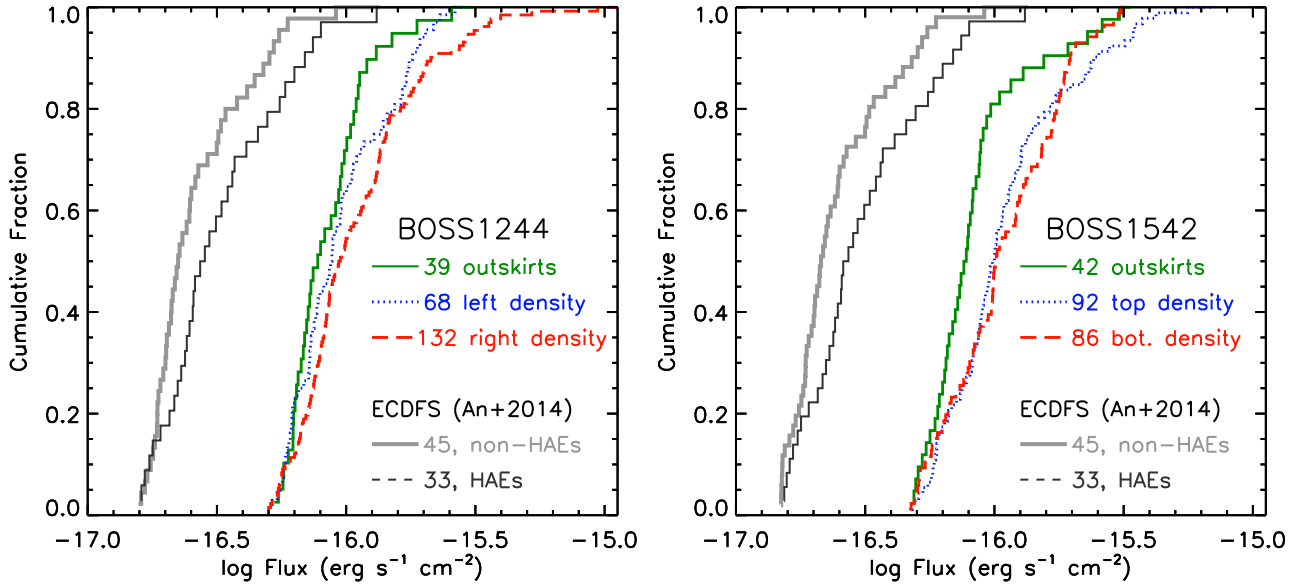
Figure 7. Cumulative fraction of the observed line fluxes in different parts of BOSS1244 (left) and BOSS1542 (right). The descriptions of these parts are given in the text. The numbers of line emitters in these parts are presented. The line emitters in the ECDFS field from An et al. (2014) are taken as representative of the general field at $z = 2.24$. Here the detection in the ECDFS is limited to the same depths of the $H_2S(1)$ and K_s observations in BOSS1244. The cumulative curves of HAEs (black) and of non-HAEs (grey) in the ECDFS are shifted by -0.5 dex for clarity. We can see that the line fluxes of HAEs are relatively higher (by $\sim$0.1 dex) than those of non-HAEs in the ECDFS. In BOSS1244 and BOSS1542, the emitters in the high-density regions also have emission lines relatively brighter than the emitters in the outskirts. We note that a correction of [N II]/Hα= 0.117 is needed to obtain Hα. The flux of Hα at $z = 2.24$ can be converted to luminosity by adding 58.58 dex and the extinction correction for $A(H\alpha) = 1$ mag will increase the luminosity by 0.4 dex.

density made of 68 objects is an extended and weak concentration, and the right density hosts all emitters with $\log f_{\text{line}} > -15.6$. In BOSS1542, the line fluxes of the emitters in both the top and bottom density are statistically higher by typically $\sim$0.1 dex in comparison with those of the emitters in the outskirts; the top density contains more objects with high line fluxes. We can conclude that the emitters in the high-density regions have line fluxes globally higher than the emitters in the outskirts of the two MAMMOTH overdensities, following the difference of the line flux distributions between HAEs and non-HAEs in the ECDFS.

Moreover, the cumulative distribution of line fluxes of the emitters in the outskirts appears analogous to that of the non-HAEs in the ECDFS. We use the Kolmogorov−Smirnov (K−S) test to quantify the probability that two samples are drawn from the same population. It measures the significance level of consistency of two cumulative distributions. The p-value of the K−S test is 0.59, 0.06 and 0.001 when comparing the non-HAEs in the ECDFS with the emitters in the outskirts, left-density and right-density regions, respectively, of BOSS1244, and 0.38, 1.45×10^{-5} and 5.40×10^{-5} with these in the outskirts, top-density and bottom-density regions of BOSS1542. Similarly, the K−S test yields 0.26, 0.96 and 0.97 for the HAEs in the ECDFS in comparison with the three emitter samples in BOSS1244, and 0.19, 0.22 and 0.24 with the three emitter samples in BOSS1542. These results show that the emitters in the outskirts of two MAMMOTH overdensities satisfy the line flux distribution of the non-HAEs in the ECDFS at a high significance level, and their line flux distribution inevitably differs from that of the HAEs. However, the emitters in the high-density regions exhibit similar line flux distribution to the HAEs in the ECDFS. The consistency is weaker for BOSS1542 because this giant filamentary structure contains more emitters with high line fluxes. These results support

our conclusion that the high-density structures are dominated by HAEs at $z = 2.24$ and are unlikely to be significantly contaminated by foreground or background emitters. Again, spectroscopic observations will play a key role in characterizing these density substructures.

The large-scale overdensities found at $z > 2$ often exhibit filamentary structures or multiple components. The $z = 3.1$ overdensity in the SSA22 field consists of three extended filamentary structures (Matsuda et al. 2005; Yamada et al. 2012). Lee et al. (2014) reported a structure over 50 cMpc containing multiple protoclusters at $z = 3.78$ in the Boötes field and these protoclusters are connected with filamentary structures. A multicomponent protosupercluster at $z = 2.45$ has been found in the COSMOS field, expanding over >60 cMpc in all three dimensions (Cucciati et al. 2018). The massive protocluster at $z = 3.13$ in the D1 field of the CFHT Legacy Survey (CFHTLS) also exhibits multiple density components traced by Lyα emitters and Lyman break galaxies (Toshikawa et al. 2016; Shi et al. 2019). The first overdensity discovered using the MAMMOTH technique, BOSS1441 at $z = 2.32$, is an elongated large-scale structure of Lyα emitters on a scale of 15 cMpc (Cai et al. 2017). Traced mostly by Lyα emitters or Lyman break galaxies, these large-scale structures represent the extremely massive overdensities at $z \sim$ 2–4. In simulations large-scale overdensities of multiple components at $z > 2$ are found to be very rare, being solely the progenitors of massive structures of $\sim 10^{15}$ M$_\odot$ (Topping et al. 2018).

4.3 Hα luminosity function

It is essential to derive the luminosity function (LF) of the intrinsic Hα luminosity that can be used as an SFR indicator of a galaxy. This will allow us to make a direct comparison of our overdensities with

the general field and to examine the distribution of star formation in member galaxies of the overdensities. Below we describe the procedure for building the Hα LF. This is done in the same way for both BOSS1244 and BOSS1542.

4.3.1 Estimate of Hα luminosities

We calculate Hα+[N II] flux density (erg s^{-1} cm^{-2}) from the narrow-band excess $K_s-H_2S(1)$ and K_s total magnitude using the formula

$$F = \Delta H_2S(1) \times \frac{f_{H_2S(1)} - f_{K_s}}{1 - \Delta H_2S(1)/\Delta K_s}, \qquad (2)$$

where $f_{H_2S(1)}$ and f_{K_s} refer to flux densities given in the units of erg s^{-1} cm^{-2} Å^{-1} in the $H_2S(1)$ and K_s bands with bandwidths $\Delta H_2S(1) = 293$ Å and $\Delta K_s = 3250$ Å, respectively. Following An et al. (2014), we use [N II]/Hα = 0.117 to subtract the contribution of [N II]λλ6548, 6583 and to obtain the observed Hα line flux. The selection cut EW > 45 Å (i.e. $K_s-H_2S(1) > 0.39$ mag) together with the 5 σ depths of $H_2S(1) = 22.6$ mag and $K_s = 23.3$ mag (BOSS1244) determines an Hα flux detection limit of $> 2.5 \times 10^{-17}$ erg s^{-1} cm^{-2}. We adopt $D = 17,892\,h^{-1}$ Mpc as the luminosity distance to $z = 2.246$ to convert the Hα line flux into the observed Hα luminosity for all HAEs. Following Sobral et al. (2013), a constant extinction correction $A(H\alpha) = 1$ mag is applied to obtain the intrinsic Hα luminosity, which is used to construct the Hα luminosity function.

We derive the SFR from the intrinsic Hα luminosity following $\log(\mathrm{SFR}/\mathrm{M}_\odot\,\mathrm{yr}^{-1}) = \log(L_{H\alpha}) - 41.27$ given in Kennicutt & Evans (2012). The Hα flux detection limit corresponds to an SFR of $5.1\,\mathrm{M}_\odot\,\mathrm{yr}^{-1}$.

4.3.2 The intrinsic EW distribution

The next step is to derive the completeness across the intrinsic Hα luminosity through fully accounting for detection limits and photometric selection. As shown in Fig. 5, our sample selection is done with the $K_s-H_2S(1)$ excess (i.e. an EW) together with source magnitudes in the two bands. We realize that HAEs of a given Hα luminosity can be bright with low EWs or faint with large EWs. We thus need to know the intrinsic EW distribution and to quantify the noise effects on our sample selection. A lognormal distribution of EW is adopted for the observed Hα+[N II] (Ly et al. 2011) to conduct Monte Carlo simulations and estimate completeness for individual Hα luminosity bins of our data.

To determine the intrinsic EW distribution of Hα+[N II] fluxes of our sample HAEs, we use a method based on a maximum likelihood algorithm (see An et al. 2014, for more details). We generate lognormal EW distributions having the mean $\log(EW_{\rm rest})$ ranging between 1.8 and 2.3 and the dispersion $\sigma[\log(EW_{\rm rest}/\text{Å})]$ ranging between 0.15 and 0.65 with a step of 0.1 dex for both parameters. We assume that Hα+[N II] flux is uncorrelated with its EW. This allows us to produce $H_2S(1)$ and K_s magnitudes by randomly assigning EWs that obey a given distribution to the observed Hα+[N II] fluxes. Accounting for the background noises from our $H_2S(1)$ and K_s images, we apply the $H_2S(1)-K_s$ selection criteria to the simulated galaxies. For each of input intrinsic EW distributions, the 'observed' EW distribution is modelled to match our $H_2S(1)$ and K_s observations. We determine the intrinsic EW distribution best matching the observed EW distribution of our sample HAEs from the modelled EW distributions using the least-squares method. The best-fitting EW distribution is described by a mean $\log(EW_{\rm rest}) = 2.00$ and a dispersion $\sigma[\log(EW_{\rm rest}/\text{Å})] = 0.35$.

4.3.3 Deriving the detection completeness

We use the Monte Carlo simulation method to generate mock catalogues of Hα emission-line galaxies satisfying a given Hα LF at $z = 2.24$. The mock catalogues are used to derive the detection completeness after accounting for the noises and detection limits in our $H_2S(1)$ and K_s observations. We adopt the Schechter function with $L^*_{H\alpha} = 10^{42.88}$, $\alpha = -1.60$ and $\log\phi^* = -1.79$ from Sobral et al. (2013) as the intrinsic Hα LF for our two overdensities. An et al. (2014) pointed out that the Hα LF has a shallower faint-end slope ($\alpha = -1.36$) and mirrors the stellar mass function of SFGs at the same redshift. They derived the extinction correction for individual HAEs and recovered some heavily attenuated HAEs, which appear to be less luminous, from the observed Hα luminosity. However, we are currently unable to derive extinction for individual HAEs because of the lack of multiwavelength observations. In Sobral et al. (2013), a constant correction $A(H\alpha) = 1$ mag was applied for all Hα galaxies. We adopt their Hα LF and extinction correction in our analysis.

The $H_2S(1)$ filter centres at $\lambda_c = 2.130\,\mu$m with an effective width of $\Delta\lambda = 0.0293\,\mu$m, and probes Hα in a redshift bin of $2.225 < z < 2.267$. We use this redshift bin to compute the effective volume for our sample. The extended wing of the filter transmission curve may allow brighter (rather than fainter) emission-line objects to be detectable. We thus simulate HAEs over $2.20 < z < 2.29$ in order to estimate the contribution of the HAEs out of the redshift bin $2.225 < z < 2.267$. The redshift span of $2.20 < z < 2.29$ is divided into 30 bins. In each redshift bin, one million mock galaxies are generated to have Hα luminosities spreading into 500 bins in the range $40 < \log(L_{H\alpha}/\mathrm{erg\,s}^{-1}) < 50$ and following the given LF. There are typically ~2000 simulated galaxies in each bin. A flux ratio of [N II]/Hα = 0.117 is adopted to account for the contribution of [N II] to Hα. The Hα lines of these mock galaxies are simulated with a Gaussian profile of $\sigma = 200\,\mathrm{km\,s}^{-1}$ at given redshifts, and convolved with the $H_2S(1)$ filter transmission curve to yield the observed Hα+[N II] fluxes for the mock galaxies.

Similarly, we randomly assign EWs obeying the best-fitting EW distribution to the simulated galaxies of given Hα+[N II] fluxes and we determine their $H_2S(1)$ and K_s magnitudes after including photon noise and sky background noises from the corresponding images. Applying the same selection criteria as presented in Fig. 5, we derive the fraction of the selected mock galaxies in all intrinsic Hα luminosity bins. Then we obtain the completeness function, as shown Fig. 8. As we can see, the completeness declines rapidly at $\log(L_{H\alpha}/\mathrm{erg\,s}^{-1}) < 42.8$. Here the volume correction and completeness estimate are based on the redshift bin $2.225 < z < 2.267$, and the final completeness curve accounts for all major effects involved in our observations and selection. Note that the completeness curve is insensitive to the input Schechter function in our simulations and thus the determination of the intrinsic Hα LF in our two overdensities is little affected by the input function in deriving detection completeness.

4.3.4 Determining the Hα luminosity function

As shown in Section 4.1, we estimate 48 ± 2 non-HAEs for both of our emitter samples and derive that 196 ± 2 of 244 (80 per cent) and 175 ± 2 of 223 (78 per cent) emission-line objects are HAEs at $2.225 < z < 2.267$ belonging to the massive overdensities BOSS1244 and BOSS1542, respectively. Of these objects, five QSOs in BOSS1244 and three QSOs in BOSS1542 are excluded. With current data and observations, we are unable to recognize non-HAEs from the HAEs. We subtract the non-HAEs in a statistical way when constructing Hα
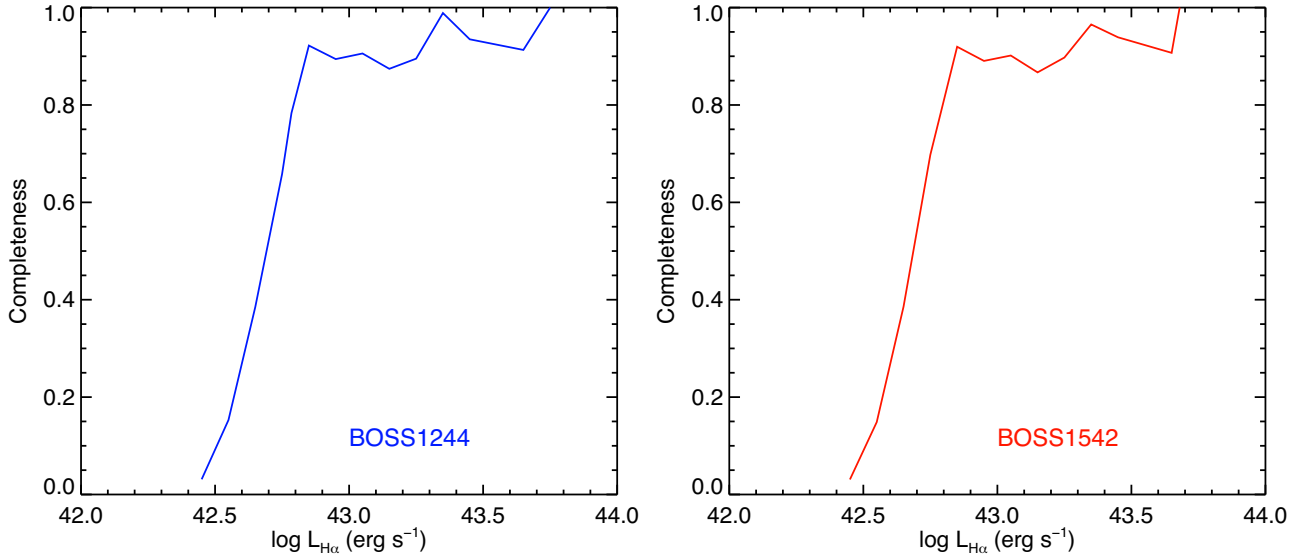
Figure 8. Completeness as a function of the intrinsic Hα luminosity in BOSS1244 (left) and in BOSS1542 (right).

LF. It has been shown that the line flux distribution of the emitters in the outskirts of the two overdensities differs from that of the emitters in the dense regions, following the difference between the non-HAEs and HAEs in the ECDFS. It is reasonable to assume that the outskirts contain more non-HAEs and the high-density regions are dominated by HAEs. Still, the outskirts contain a fraction of HAEs partially contributed by the dense structures, although the outskirts hold the information of true non-HAEs in the target fields. In practice, we remove 48 emitters following the line flux distribution of the non-HAEs in the ECDFS (see Fig. 7) from our samples and we use the remaining 143 objects in BOSS1244 and 124 objects in BOSS1542 to derive the Hα LF. The difference of the line flux distribution between the non-HAEs in the ECDFS and the outskirts of the two overdensities does not cause noticeable changes to the line flux distribution of the remaining objects. We point out that non-HAEs represent only ∼20 per cent of the total emitters in the two overdensity fields. The uncertainty in estimating the number of the non-HAEs should have no significant effect on our results of the Hα LFs. The observed line fluxes of these non-HAEs tend to be relatively fainter and the vast majority (>85 per cent) of them have line fluxes of $\log(f_{\mathrm{line}}) < -15.9$. The error in correction for non-HAEs influences the faint end of the intrinsic Hα LF at $\log L_{\mathrm{H}\alpha} < 43.05$.

Our sample of HAEs spreads in $2.225 < z < 2.267$ over an area of 417 and 399 arcmin², giving a volume of 58 154 and 55 644 h^{-3} Mpc³ in BOSS1244 and BOSS1542, respectively. We divide the sample HAEs into six Hα luminosity bins over $42.6 < \log(L_{\mathrm{H}\alpha}) < 43.8$. We calculate the volume density of HAEs at given bins after correcting for the completeness, and we obtain our Hα LF data points. The Poisson noise is adopted as their errors. A Schechter function (Schechter 1976) is used to fit the data points:

$$\Phi(\log L)\,\mathrm{d}(\log L) = \ln(10)\,\Phi^{\star}\,10^{(\alpha+1)(\log L - \log L^{\star})}$$

$$\times \exp[-10^{\log L - \log L^{\star}}]\,\mathrm{d}(\log L). \qquad (3)$$

Here, $L^{\star}$ refers to the characteristic luminosity, $\Phi^{\star}$ is the characteristic density and α represents the power-law index of the faint end. The χ^2 minimization method is utilized to determine the best-fitting parameters, giving $\log L^{\star} = 42.91$, $\Phi^{\star} = 0.0078$ and $\alpha = -1.60$

for BOSS1244, and $\log L^{\star} = 43.13$, $\Phi^{\star} = 0.0032$ and $\alpha = -1.68$ for BOSS1542.

We show the Hα LFs of our two overdensities at $z = 2.24$ in Fig. 9. The Hα LF at $z = 2.23$ of the general field from Sobral et al. (2013) is also included for comparison. Note that our Hα LFs of BOSS1244 and BOSS1542 are scaled down by a best-matched factor of 6.3 and 5.6, respectively, consistent with $1 + \delta_{\mathrm{gal}} = 6.6 \pm 0.3$ and 5.9 ± 0.3 within the uncertainties. It is clear that the Hα LF of BOSS1244 agrees well with that of the general field, while the Hα LF of BOSS1542 exhibits a prominent excess at the high end. As can be seen from Fig. 9, this excess is not due to an underestimate of the overdensity factor because the two data points at $\log(L_{\mathrm{H}\alpha}) < 43$ are already below the Hα LF of the general field. There are 10 and 14 objects with $\log L_{\mathrm{H}\alpha} > 43.4$, accounting for 5 and 8 per cent of HAEs in BOSS1244 and BOSS1542, respectively. Only two objects have Hα with $\log L_{\mathrm{H}\alpha} > 43.6$ in each of the two overdensities. These objects make the two data points at $\log L_{\mathrm{H}\alpha} > 43.4$, and thus are critical to the high end of the Hα LF. Compared with 10 objects (5 per cent of the total) in BOSS1242, the high end of BOSS1542 consists of 14 objects (8 per cent of the total), showing an excess of 50 per cent for $\log L_{\mathrm{H}\alpha} > 43.4$ at a $2\,\sigma$ confidence.

We caution that our samples of HAEs possibly contain AGNs that are less luminous than quasars but significantly contribute to Hα luminosity and thus increase the high end of the Hα LF of SFGs that we want to obtain. Based on the 4 Ms Chandra X-ray observations, An et al. (2014) identified three X-ray-detected AGNs among 56 HAEs in the ECDFS field, which are exclusively the brightest HAEs with $\log(L_{\mathrm{H}\alpha}) > 43.5$. This suggests an AGN fraction of 9 per cent in the field when limiting HAEs to our detection depths. The fraction of AGNs in high-redshift protoclusters reported in previous studies is typically several per cent but with large scatter, depending on the evolutionary stage, total mass and gas fraction of the protoclusters (e.g. Macuga et al. 2019). The two bins at the high end of Hα LF contain 5 and 8 per cent of HAEs in BOSS1244 and BOSS1542, respectively, comparable with the reported AGN fractions in the protoclusters. We caution that the two luminosity bins at $\log L_{\mathrm{H}\alpha} > 43.4$ in our Hα LFs might be seriously contaminated by AGNs. We lack the X-ray observations to detect AGNs and to remove them from our samples of HAEs.
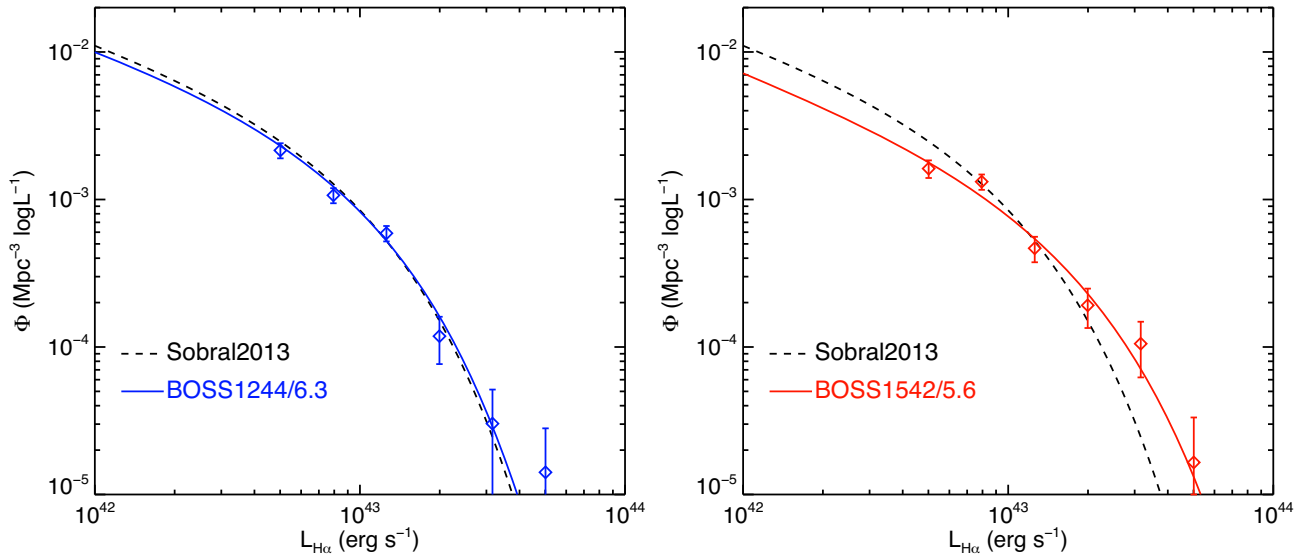
Figure 9. Comparison of the Hα LFs in BOSS1244 (left) and in BOSS1542 (right) with that in the general field at $z = 2.23$ from Sobral et al. (2013). The Hα LFs of the two overdensities are scaled down by a factor of 6.3 and 5.6, respectively. Interestingly, the Hα LF of BOSS1542 shows an excess at $\log(L_{H\alpha}) >$ 43.3. This excess is not seen in BOSS1244.

5 CONCLUSIONS

We used the WIRCam instrument mounted on the CFHT to carry out deep NIR imaging observations through narrow-band $H_2S(1)$ and broad-band K_s filters for identifying Hα emission-line galaxies at $z = 2.246 \pm 0.021$ in two 20×20 arcmin^2 fields, BOSS1244 and BOSS1542, where massive MAMMOTH overdensites are indicated by most extreme groups of IGM Lyα absorption systems at $z =$ 2.24 over a scale of $\sim 20\,h^{-1}$ cMpc imprinted on the available SDSS-III spectra. The two overdensity candidates represent the extremely massive ones selected over a sky coverage of $10\,000\,\mathrm{deg}^2$.

There are 244 and 223 emission-line objects selected with rest-frame EW > 45 Å and $H_2S(1) < 22.5$ mag over an effective area of 417 and 399 arcmin^2 to the $5\,\sigma$ depths of $H_2S(1) = 22.58$ and 22.67 mag and $K_s = 23.29$ and 23.23 mag in BOSS1244 and BOSS1542, respectively. Of these, 196 ± 2 (80 per cent) and 175 ± 2 (78 per cent) are estimated to be HAEs at $z = 2.24$ in the two overdensities, in comparison with 36–40 per cent of emission-line objects that are estimated to be HAEs in the general field. We estimate the global overdensity factor of HAEs to be $\delta_{gal} = 5.6 \pm 0.3$ and 4.9 ± 0.3 in a volume of $54 \times 32 \times 32\,h^{-1}$ cMpc^3 for BOSS1244 and BOSS1542, respectively. The overdensity factor would increase two to three times if focusing on the high-density regions with a scale of 10–15 cMpc. The striking excess of HAEs is convincing evidence that the two overdensities are very massive structures at $z > 2$.

The HAE density maps reveal that the two overdense structures span over $30\,h^{-1}$ cMpc with distinct morphologies. BOSS1244 contains two components: one low-density component connected to the other elongated high-density component. The high-density substructure has $\delta_{gal} = 15$. If confirmed to be one physical structure, it would collapse into a present-day massive cluster, as suggested by simulations. In contrast, BOSS1542 manifests as a large-scale filamentary structure.

We subtract the contribution of possible non-HAEs from our sample of HAE candidates in a statistical manner and construct Hα luminosity functions for our two overdensities. We find that the Hα luminosity functions are well fitted with a Schechter function. After correcting for the overdensity factor, BOSS1244's Hα LF

agrees well with that of the general field at the same epoch from Sobral et al. (2013). The Hα LF of BOSS1542, however, shows an excess of HAEs at the high-luminosity end at a $2\,\sigma$ confidence. Interestingly, these HAEs with $\log L_{H\alpha} > 43.4$ are mostly located at the intermediate-density regions other than the density peak area. These suggest that star formation is not seriously influenced by the extremely dense environment in BOSS1244, and even plausibly enhanced in BOSS1542, although our data are unable to probe AGNs and quiescent member galaxies. Taken together with the unbounded structures, we infer that the two $z = 2.24$ massive overdensities were undergoing a rapid assembly.

Our results denote that the two massive overdensities at $z = 2.24$ are extremely interesting targets to investigate the environment dependence of galaxy evolution, to address both the environmental mechanisms for triggering quasar activities and the coevolution between SMBHs and galaxies, and to provide constraints on hierarchical structure formation models and the standard cosmological model. We will address these issues in future papers.

search Council (NRC) of Canada, the Institut National des Sciences de l'Univers of the Centre National de la Recherche Scientifique of France, and the University of Hawaii.

DATA AVAILABILITY

The data underlying this article will be shared on reasonable request to the corresponding author.

REFERENCES

Alam S. et al., 2015, ApJS, 219, 12
Allen S. W., Evrard A. E., Mantz A. B., 2011, ARA&A, 49, 409
An F. X., Zheng X. Z., Meng Y., Chen Y., Wen Z., Lü G., 2013, Science China Physics, Mechanics and Astronomy, 56, 2226
An F. X. et al., 2014, ApJ, 784, 152
Angulo R. E., Springel V., White S. D. M., Cole S., Jenkins A., Baugh C. M., Frenk C. S., 2012, MNRAS, 425, 2722
Berrier J. C., Stewart K. R., Bullock J. S., Purcell C. W., Barton E. J., Wechsler R. H., 2009, ApJ, 690, 1292
Bertin E., Arnouts S., 1996, A&AS, 117, 393
Blanton M. R., Moustakas J., 2009, ARA&A, 47, 159
Bleem L. E. et al., 2015, ApJS, 216, 27
Bond J. R., Kofman L., Pogosyan D., 1996, Nature, 380, 603
Boylan-Kolchin M., Springel V., White S. D. M., Jenkins A., Lemson G., 2009, MNRAS, 398, 1150
Brodwin M. et al., 2013, ApJ, 779, 138
Cai Z. et al., 2016, ApJ, 833, 135
Cai Z. et al., 2017, ApJ, 839, 131
Casey C. M., 2016, ApJ, 824, 36
Casey C. M. et al., 2015, ApJ, 808, L33
Chiang Y-K., Overzier R., Gebhardt K., 2013, ApJ, 779, 127
Chiang Y-K. et al., 2015, ApJ, 808, 37
Chiang Y-K., Overzier R. A., Gebhardt K., Henriques B., 2017, ApJ, 844, L23
Contini E., De Lucia G., Hatch N., Borgani S., Kang X., 2016, MNRAS, 456, 1924
Coogan R. T. et al., 2018, MNRAS, 479, 703
Cucciati O. et al., 2014, A&A, 570, A16
Cucciati O. et al., 2018, A&A, 619, A49
Dannerbauer H. et al., 2014, A&A, 570, A55
De Lucia G., Blaizot J., 2007, MNRAS, 375, 2
Digby-North J. A. et al., 2010, MNRAS, 407, 846
Dressler A., 1984, ARA&A, 22, 185
Elbaz D. et al., 2007, A&A, 468, 33
Gilbank D. G., Gladders M. D., Yee H. K. C., Hsieh B. C., 2011, AJ, 141, 94
Hayashi M., Kodama T., Tadaki K-i., Koyama Y., Tanaka I., 2012, ApJ, 757, 15
Hayashi M., Kodama T., Tanaka I., Shimakawa R., Koyama Y., Tadaki K-i., Suzuki T. L., Yamamoto M., 2016, ApJ, 826, L28
Hayes M., Schaerer D., Östlin G., 2010, A&A, 509, L5
Hine N. K., Geach J. E., Alexander D. M., Lehmer B. D., Chapman S. C., Matsuda Y., 2016, MNRAS, 455, 2363
Kauffmann G., White S. D. M., Heckman T. M., Ménard B., Brinchmann J., Charlot S., Tremonti C., Brinkmann J., 2004, MNRAS, 353, 713
Kennicutt R. C., Evans N. J., 2012, ARA&A, 50, 531
Kollmeier J. A., Weinberg D. H., Davé R., Katz N., 2003, ApJ, 594, 75
Koyama Y., Kodama T., Tadaki K-i., Hayashi M., Tanaka M., Smail I., Tanaka I., Kurk J., 2013, MNRAS, 428, 1551
Kravtsov A. V., Borgani S., 2012, ARA&A, 50, 353
Krishnan C. et al., 2017, MNRAS, 470, 2170
Kroupa P., 2001, MNRAS, 322, 231
Lee J. C. et al., 2012, PASP, 124, 782
Lee K-S., Dey A., Hong S., Reddy N., Wilson C., Jannuzi B. T., Inami H., Gonzalez A. H., 2014, ApJ, 796, 126
Lehmer B. D. et al., 2009, ApJ, 691, 687
Lemaux B. C. et al., 2014, A&A, 572, A41
Lidman C. et al., 2012, MNRAS, 427, 550
Lovell C. C., Thomas P. A., Wilkins S. M., 2018, MNRAS, 474, 4612
Ly C., Lee J. C., Dale D. A., Momcheva I., Salim S., Staudaher S., Moore C. A., Finn R., 2011, ApJ, 726, 109
Macuga M. et al., 2019, ApJ, 874, 54
Madau P., Dickinson M., 2014, ARA&A, 52, 415
Martini P. et al., 2013, ApJ, 768, 1
Matsuda Y. et al., 2005, ApJ, 634, L125
Muldrew S. I., Hatch N. A., Cooke E. A., 2015, MNRAS, 452, 2528
Noble A. G. et al., 2017, ApJ, 842, L21
Onoue M. et al., 2018, PASJ, 70, S31
Overzier R. A., 2016, A&AR, 24, 14
Owers M. S. et al., 2019, ApJ, 873, 52
Schaye J. et al., 2015, MNRAS, 446, 521
Schechter P., 1976, ApJ, 203, 297
Shi K. et al., 2019, ApJ, 879, 9
Shimakawa R. et al., 2018a, MNRAS, 473, 1977
Shimakawa R. et al., 2018b, MNRAS, 481, 5630
Sobral D., Smail I., Best P. N., Geach J. E., Matsuda Y., Stott J. P., Cirasuolo M., Kurk J., 2013, MNRAS, 428, 1128
Strazzullo V. et al., 2016, ApJ, 833, L20
Tanaka M., De Breuck C., Venemans B., Kurk J., 2010, A&A, 518, A18
Thomas D., Maraston C., Bender R., Mendes de Oliveira C., 2005, ApJ, 621, 673
Topping M. W., Shapley A. E., Steidel C. C., Naoz S., Primack J. R., 2018, ApJ, 852, 134
Toshikawa J. et al., 2016, ApJ, 826, 114
Tran K-V. H. et al., 2015, ApJ, 811, 28
Umehata H. et al., 2015, ApJ, 815, L8
Venemans B. P. et al., 2007, A&A, 461, 823
von der Linden A., Wild V., Kauffmann G., White S. D. M., Weinmann S., 2010, MNRAS, 404, 1231
Wang T. et al., 2016, ApJ, 828, 56
Wang T. et al., 2018, ApJ, 867, L29
Watson C. et al., 2019, ApJ, 874, 63
Yamada T., Nakamura Y., Matsuda Y., Hayashino T., Yamauchi R., Morimoto N., Kousai K., Umemura M., 2012, AJ, 143, 79
Yuan T. et al., 2014, ApJ, 795, L20
Zavala J. A. et al., 2019, ApJ, 887, 183

This paper has been typeset from a TeX/LaTeX file prepared by the author.